communications materials

A Nature Portfolio journal

Article

https://doi.org/10.1038/s43246-025-00862-8

Mathematical approaches for track analysis and process optimization in additive manufacturing

Check for updates

Mahdi Alishavandi [1,2] ✉, Rahmi Ünal [1,2] & Metin Uymaz Salamci [1,2]

Additive manufacturing demands precise control of track formation and process parameters. Here we show a unified mathematical framework that links key variables to track geometry: we derive analytical expressions for solid and liquid contact angles, introduce dimensionless wetting shape factors to compute segment area and volume, and develop quadratic models relating powder layer thickness to track width and height. We further present a normalized enthalpy formulation that correlates laser energy input with melt pool depth and absorption, enabling prediction of the transition from single-track behavior to steady-state and the derivation of optimal hatch spacing. Validation on IN625, IN738LC, AA1000, and Al10SiMg powders reveals excellent agreement between predicted and measured track morphologies in conduction and keyhole modes. Although tailored for laser powder bed fusion, this framework is broadly applicable across additive manufacturing processes, offering a robust tool for process optimization, in situ monitoring, and quality control.

Additive manufacturing (AM) is a precise, track-by-track, and layer-by-layer buildup process controlled by the characteristics of each deposited track[1]. Despite its precision, challenges related to reproducibility and control at the mesoscale persist, presenting significant obstacles that must be addressed to enhance the fabrication process[2].

While many scientists adopt a top-down approach by printing bulk samples to study process parameter optimization, the bottom-up approach, starting with single tracks, progressing to multitrack, and finally multilayers, offers several advantages. This method provides a more detailed understanding of track behavior, facilitates more accurate simulations, and allows for a more precise interpretation of the underlying phenomena that influence track formation. As a result, it enhances the ability to simulate and predict desired process parameters with greater precision[3,4].

To address these challenges, a bottom-up approach, starting with a single track and progressing to multitrack and multilayer structures, offers a logical method for uncovering and understanding the underlying effects influencing the final part's quality from the mesoscale to the macroscale[1,3]. By focusing on the single-track approach, researchers can gain valuable insights into the intricate relationships between various geometric parameters of the track, allowing for the optimization of process parameters to achieve the desired microstructural and mechanical properties[5].

The primary objective of studying single tracks is to accurately represent the behavior of bulk tracks during the manufacturing process and to identify strategies for overcoming defects in the final parts[6–8]. By manipulating the height, width, depth, and contact angle of a single track, it is possible to tailor the properties of the printed bulk sample to meet specific requirements[9]. For example, controlling these parameters can help achieve optimal surface finish in medical applications, enhance fatigue behavior in aerospace components, and minimize residual stress in crack-susceptible alloys across various AM processes[10].

Early researchers developed mathematical models to deepen our understanding of complex track formation, accurately predict temperature distributions, and elucidate their impact on melt pool characteristics. Rosenthal made one of the earliest attempts to mathematically model the temperature distribution and melt pool characteristics in 1946[11]. Rosenthal assumed a point-shaped heat source on a plate and derived equations for temperature distributions and cooling rates in conduction mode. His work provided a foundation for calculating the melt pool size in welding, which can also be applied to AM. However, Rosenthal's model has limitations, particularly in predicting the weld pool shape.

Eagar and Tsai later improved Rosenthal's model using a Gaussian heat source instead of a point source[12]. This modification allowed for more accurate predictions of weld pool shapes, especially regarding width. They presented dimensionless solutions applicable to different materials and welding conditions. Unlike Rosenthal's model, Eagar and Tsai's approach provides detailed information on weld pool shape, including width, depth, and area.

Hann et al.[13] subsequently developed a simple mathematical model to predict laser weld properties via a normalized enthalpy (NE) approach. They

[1]Additive Manufacturing Technologies Application and Research Center (EKTAM), Gazi University, Ankara, Turkey. [2]Department of Mechanical Engineering, Gazi University, Ankara, Turkey. ✉e-mail: Mahdi.Alishavandi@Gazi.edu.tr

established a relationship between the weld depth and an NE parameter, which combines laser and material properties. Their findings showed that the normalized weld depth correlates well with the NE across various materials and welding conditions. Additionally, their model could predict transitions between conduction and keyhole welding modes on the basis of critical enthalpy values, and they related the weld width and aspect ratio to the NE.

These early models were developed for autogenous welding modes without incorporating powder, which limits their direct application to AM[14]. Recognizing this gap, researchers later sought to adapt and extend these models for AM processes. King et al.[15], for instance, incorporated the concept of NE into laser powder bed fusion (LPBF) to identify the threshold for the transition from conduction mode to keyhole mode melting in terms of an NE parameter.

Understanding the track morphology in both solid and liquid states is crucial for tailoring the properties of AM products[16]. Recognizing that prior studies have largely relied on empirical correlations without a unified theoretical basis, this work fills a critical gap by establishing a rigorous mathematical framework that links track attributes—such as width, height, contact angle, and powder layer thickness—to material and laser parameters. By leveraging geometry, analytical geometry, calculus, algebra, and trigonometry, we derive explicit relationships that account for acute and obtuse wetting scenarios, introduce novel dimensionless wetting shape factors, and develop quadratic models to predict track dimensions and maximum hatch spacing. Moreover, our framework incorporates the concept of NE to effectively relate the energy input to the melt pool depth and absorption characteristics, offering a more holistic understanding of the process. Comprehensive experimental validation using IN625, IN738LC, AA1000, and Al10SiMg confirms the accuracy of these models, reinforcing their applicability and paving the way for enhanced process control and in-situ monitoring in AM.

Mathematical modeling

Geometric relationships among the wetting angle, width, and height

Analyzing a solidified single track's transverse cross-section aims to establish relationships among the track's width, height, radius, and contact angle. Two distinct scenarios emerge based on the contact angle between the track and the substrate, as shown in Fig. 1. In the first case, an acute contact angle is observed when the substrate (represented by a secant line) intersects the circle, creating a minor segment. The second scenario involves an obtuse contact angle, where the secant line forms a major circular segment. The derived equations elucidate the relationships among the width, height, and contact angle of the solidified track on the substrate. Furthermore, these equations provide insights into the fitted circle of wetting. This circular approximation is justified by considering the bond number (Bd), also known as the Eötvös number, a dimensionless parameter defined as the ratio of the buoyancy force to the surface tension force, which is much less than 1 in this context, as shown in Section "Liquid state track properties", Eq. (95). Consequently, the gravity force becomes negligible, and the track shape consistently forms a circular segment with radius R, where R represents the circle radius fitted to the track surface.

The nomenclature used in this study is presented in Table 1. Figure 1 illustrates the two scenarios representing the solidified track on the substrate. What follows is a step-by-step, detailed derivation of the track properties to establish the relationships among the height (H), width (W), radius (R), and contact angle (θ) of the track.

Case (I): acute contact angle <90°

The apothem of the minor segment is related to the circle's radius (R) and track height (H) and is also expressed in terms of the radius and the cosine of the contact angle (θ):

$$Apothem(a_{minor}) = Radius(R) - Sagitta(H) = R\cos(\theta) \tag{1}$$

The cosine of the contact angle is expressed in terms of the height and radius:

$$\cos(\theta) = \frac{R-H}{R} = 1 - \frac{H}{R} \tag{2}$$

Derived from the cosine relationship, the radius is given in terms of the height and contact angle:

$$R = \frac{H}{1-\cos(\theta)} \tag{3}$$

The sine of the contact angle relates the half-width ($W/2$) of the track to the radius:

$$\sin(\theta) = \frac{W/2}{R} \tag{4}$$

Finally, the radius can also be expressed in terms of the width and contact angle:

$$R = \frac{W/2}{\sin(\theta)} = (W/2)\csc(\theta) \tag{5}$$

Case (II): obtuse contact angle >90°

Interestingly, the derived equations for the obtuse angle are identical to those for the acute angle when describing the relationships between width, height, radius, and contact angle.

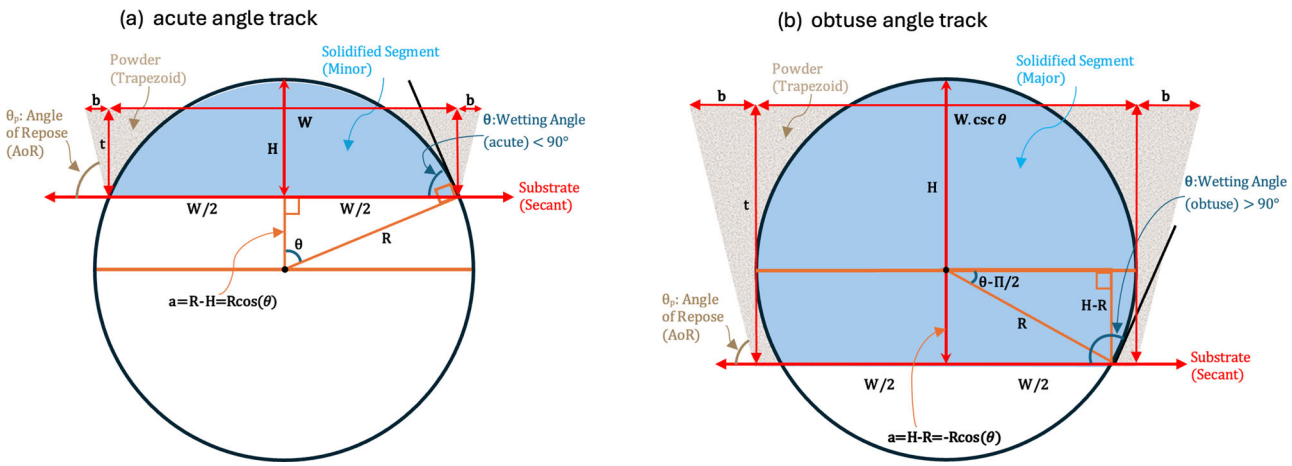


Fig. 1 | Powder layer and deposited-area melt-track geometry for acute and obtuse wetting angle tracks. a For an acute wetting angle ($\theta < 90°$), the solidified segment is the minor arc of the melt pool; **b** for an obtuse angle ($\theta < 90°$), it is the major arc.

Table 1 | Nomenclatures

Symbol	Description	Symbol	Description
a	Apothem	γ_{SL}	Solid-liquid interfacial tension
R	Radius of the wetting circle	γ_{SG}	Solid-gas interfacial tension
l	Length of the track	γ_{LG}	Liquid-gas interfacial tension
D	Depth of the track	φ, φ_W	Wetting shape factor (Width)
κ	Curvature of the track	φ_H	Wetting shape factor (Height)
t	Powder layer thickness	φ_R	Wetting shape factor (Radius)
H, H_s	Height of the solidified track (Sagitta)	S_l	Liquid arc length
H_l	Height of the track (liquid)	S_s	Solid arc length
W, W_s	Width of the solidified track	θ, θ_s	Solid contact angle
W_l	Width of the track (liquid)	θ_l	Liquid contact angle
A_s	Area of the solidified track	β	Solid-liquid angle
A_o	Overlap area	θ_p	Angle of repose (AoR)
A_p	Area of the powder	α	Thermal diffusivity
V_s	Volume of the solidified track	h	Hatch space
V_p	Volume of the powder	ρ_r	Relative density
ρ_p	Powder apparent density	ρ_l	Liquid density
ρ_s	Solidified track (true) density	h_s	Enthalpy at melting
ρ	Constant density	P	Laser power
$\rho(T)$	Temperature-dependent density	δ^*	Normalized, dimensionless depth
η	Absorptivity	Φ	Keyhole number
L_m	Latent heat of melting	NE	Normalized enthalpy
L_v	Latent heat of vaporization	L	Thermal diffusion length
ΔH	Volumetric enthalpy	$c_{p,s}$	Constant specific heat (solid)
h_s	Specific enthalpy at melting	$c_{p,\ell}$	Constant specific heat (liquid)
I	laser intensity	$c_p^{\text{liquid}}(T)$	Temp.-dependent specific heat (liquid)
v	Laser scanning speed	$c_p^{\text{solid}}(T)$	Temp.-dependent specific heat (solid)
ω_0	Laser beam radius (waist)	h_v	Specific enthalpy at vaporization
E	Laser energy	F	Fluence (laser surface energy density)
T_{vap}	Vaporization temperature	Fo	Fourier number
T_{ref}	Reference (build plate) temp.	t_{int}	Laser-material interaction time
T_m	Melting (liquidus) temperature	k	Thermal conductivity
T_b	Boiling temperature	$NE_{\eta=1}$	Normalized enthalpy assuming $\eta = 1$
T_{preheat}	Preheat temperature of the build plate	$NVED$	Normalized volumetric energy density
Bd	Bond number (Eötvös number)	H_{ss}	Steady-state track height

The apothem of the major segment is related to the track's radius and height and involves the radius and contact angle:

$$Apothem(a_{major}) = Sagitta(H) - Radius(R) = -R\cos(\theta) \tag{6}$$

The contact angle is expressed in terms of height and radius:

$$\sin\left(\theta - \frac{\pi}{2}\right) = -\cos(\theta) = \frac{H-R}{R} = \frac{H}{R} - 1 \tag{7}$$

The radius is expressed in terms of height and the contact angle:

$$R = \frac{H}{1-\cos(\theta)} \tag{8}$$

The half-width of the track is related to the radius via the sine of the contact angle:

$$\cos\left(\theta - \frac{\pi}{2}\right) = \sin(\theta) = \frac{W/2}{R} \tag{9}$$

The radius is also related to the width and contact angle through the cosecant function:

$$R = \frac{W/2}{\sin(\theta)} = (W/2)\csc(\theta) \tag{10}$$

The cosine and sine of the contact angle are connected to the height and width:

$$\cos(\theta) = 1 - \frac{\sin(\theta)H}{W/2} \tag{11}$$

The sine of the contact angle is expressed in terms of the cosine, width, and height:

$$\sin(\theta) = \frac{W/2(1-\cos(\theta))}{H} \tag{12}$$

The width is related to the height and contact angle, and an alternative form uses the cotangent of half the contact angle:

$$W = 2H\frac{\sin(\theta)}{1-\cos(\theta)} = 2H\cot(\theta/2) \tag{13}$$

The height can be expressed in terms of width and contact angle, and alternatively, the tangent of half the contact angle can be used:

$$H = W/2\frac{(1-\cos(\theta))}{\sin(\theta)} = (W/2)\tan(\theta/2) \tag{14}$$

The contact angle is expressed in terms of width, height, and radius:

$$\theta = 2\tan^{-1}\left(\frac{H}{W/2}\right) = \tan^{-1}\left(\frac{W/2}{R-H}\right) \tag{15}$$

Finally, the radius can also be expressed in terms of the width and height of the track. By combining Eqs. (2) and (4) and utilizing the identity $\cos^2(\theta) + \sin^2(\theta) = 1$, we obtain:

$$R = \frac{W^2 + 4H^2}{8H} \tag{16}$$

These equations collectively describe the geometry of the solidified track for acute and obtuse contact angles. They provide a comprehensive set of relationships between the track width (W), height (H), radius of the fitted wetting circle (R), and contact angle (θ). The derivation of these relationships allows for a comprehensive characterization of the track's geometrical shape, which is crucial for understanding and predicting the behavior of solidified tracks in various manufacturing processes such as welding,

cladding, and AM. Furthermore, these relationships can be applied and adapted for different types of surface wetting by liquid or solid droplets.

Dimensionless wetting shape factor

The formulas of this section describe various ways to calculate the area of a circular segment in Fig. 1, which is the region of a circle enclosed by a chord and an arc. The formulas account for acute and obtuse angles and provide different expressions based on the known parameters.

$$A_{s(\text{acute})} = (\theta R^2) - \left(\frac{W}{2}a\right) \tag{17}$$

$$A_{s(\text{obtuse})} = (\theta R^2) + \left(\frac{W}{2}a\right) \tag{18}$$

These formulas calculate the area of the solidified segment by subtracting (for acute angles) or adding (for obtuse angles) the triangle's area from the sector's area. Substituting the previous equations into the two equations above yields:

$$A_s = R^2\left(\frac{2\theta - \sin 2\theta}{2}\right) \tag{19}$$

By substituting Eqs. (5) and (3) into Eq. (19), alternative expressions for the area of the solidified segment can be derived as a function of the width (W) and height (H):

$$A_s = W^2\left(\frac{2\theta - \sin 2\theta}{8\sin^2\theta}\right) \tag{20}$$

$$A_s = H^2\left(\frac{2\theta - \sin 2\theta}{2(1-\cos\theta)^2}\right) \tag{21}$$

These formulas allow the calculation of the area when different parameters are known. They require one of the following: chord length (width), height, radius, plus contact angle. In this context, the φ values represent dimensionless wetting shape factors:

$$\varphi_R = \frac{2\theta - \sin 2\theta}{2} \tag{22}$$

$$\varphi_W = \varphi = \frac{2\theta - \sin 2\theta}{8\sin^2\theta} \tag{23}$$

$$\varphi_H = \frac{2\theta - \sin 2\theta}{2(1-\cos\theta)^2} \tag{24}$$

$$A_s = \varphi W^2 = \varphi_H H^2 = \varphi_R R^2 \tag{25}$$

The area of a segment can be calculated via any of these shape factors. Thus, if the contact angle θ and any one of R, W, or H is known, the segment area can be determined. The variation in different wetting shape factors (φ) concerning the wetting angle is illustrated in Fig. 2 and Supplementary Table S1.

Powder layer thickness

This section defines the relationships between various parameters of the solidified track area and the powder layer thickness (t). By applying the principle of mass conservation, the powder area (A_p) can be calculated based on the solidified track area (A_s), Eq. (25), and the powder's relative density (ρ_r):

$$m_p = m_s, \quad \rho_p V_p = \rho_s V_s, \quad V_s = \rho_r V_p, \quad A_s = \rho_r A_p$$

$$A_p = \frac{\varphi W^2}{\rho_r} \tag{26}$$

A trapezoidal shape is considered for the powder consumed in the initial track as shown in Fig. 1, solidifying into the track with a height t. In this model, θ_p represents the powder angle of repose (AoR), and b is given by $b = t\cot(\theta_p)$.

Acute angles:

$$A_p(\text{acute}) = \frac{\varphi}{\rho_r}W^2 = tW + t^2\cot(\theta_p) \tag{27}$$

This can be rearranged as follows:

$$\frac{\varphi}{\rho_r}W^2 - tW - t^2\cot(\theta_p) = 0 \tag{28}$$

Obtuse angles:

$$A_p(\text{obtuse}) = \frac{\varphi}{\rho_r}W^2 = tW\csc\theta + t^2\cot(\theta_p) \tag{29}$$

which can be rearranged to:

$$\frac{\varphi}{\rho_r}W^2 - tW\csc\theta - t^2\cot(\theta_p) = 0 \tag{30}$$

Equations (28) and (30) can also be expressed in terms of height and radius. These equations establish quadratic relationships between the powder layer thickness (t) and several critical parameters, including the track width (W), height (H), radius (R), wetting shape factor (φ), powder relative density (ρ_r), AoR (θ_p), and wetting angle (θ). These equations provide a foundational framework for calculating and understanding the geometry of powder layers and the width and height of the initial track in each layer (single-track-like) across different processes. Furthermore, by incorporating the hatch distance (h), the track properties can be determined in steady-state mode.

Given that W, H, and t are positive quantities, and that the quadratic equation discriminant (Δ) is greater than zero, these equations describe a hyperbolic curve. For each specific angle, a corresponding line (serving as an asymptote of the hyperbola) can be plotted on the $H-t$ or $W-t$ graph, representing the solutions of the quadratic equations. Consequently, 180 lines can be generated for angles ranging from 0° to 180°. It is crucial to always consider the positive solution of the quadratic equation for both the $H-t$ and $W-t$ relationships to ensure accurate representation.

Solid and liquid wetting angles

Figure 3 illustrates the wetting behavior and interfacial energy between the solid, liquid, and gas phases. In this section, we examine the relationships between the attributes of the solid and liquid tracks and derive the corresponding liquid-solid wetting shape factor relationships. The track width is assumed to remain constant during solidification ($W_s = W_l$)[17].

First, the conservation of mass between the liquid and solid states is established:

$$\rho_s W_s^2 \varphi_s L_s = \rho_l W_l^2 \varphi_l L_l \tag{31}$$

$$\varphi_l = \frac{\rho_s}{\rho_l}\varphi_s \tag{32}$$

This relationship implies that the liquid wetting angle can be determined via the contact angle of the solidified track and the densities of the liquid and solid phases. Consequently, the liquid height can be derived from the

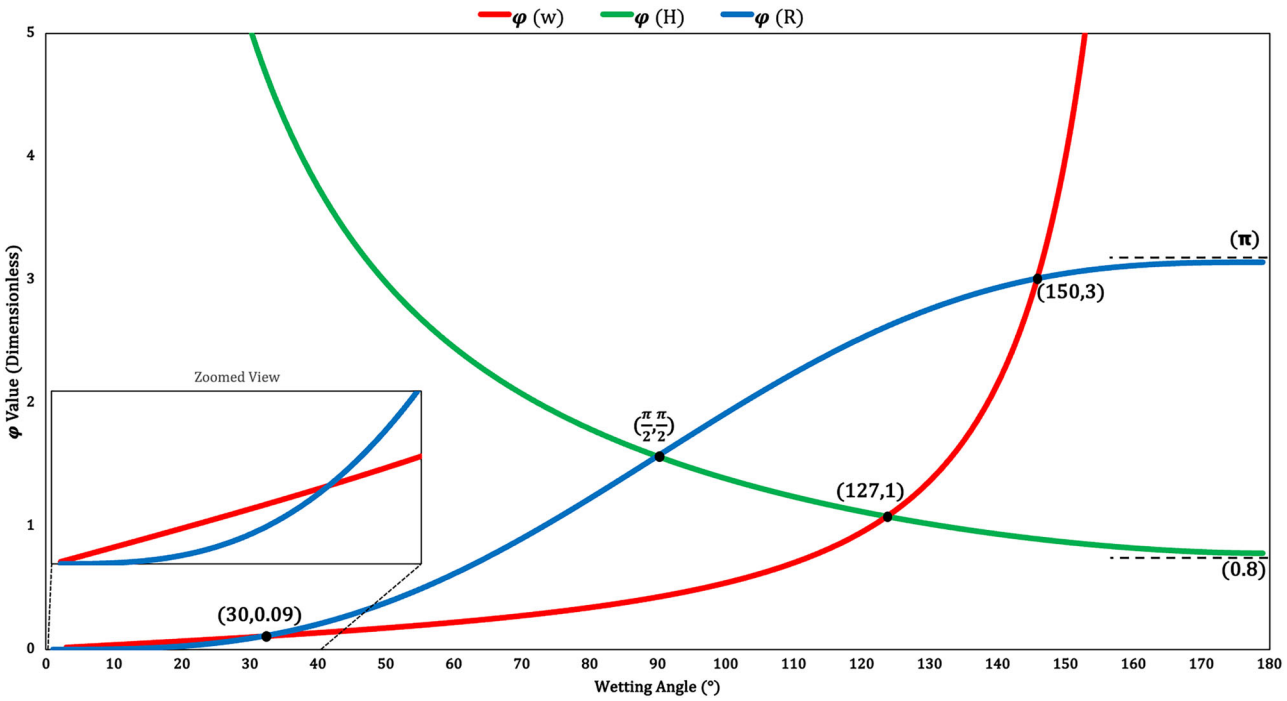


Fig. 2 | Variation in different wetting shape factors (φ_W, φ_H, φ_R) with respect to the contact angle. The plot marks significant intersection points at specific contact angles.

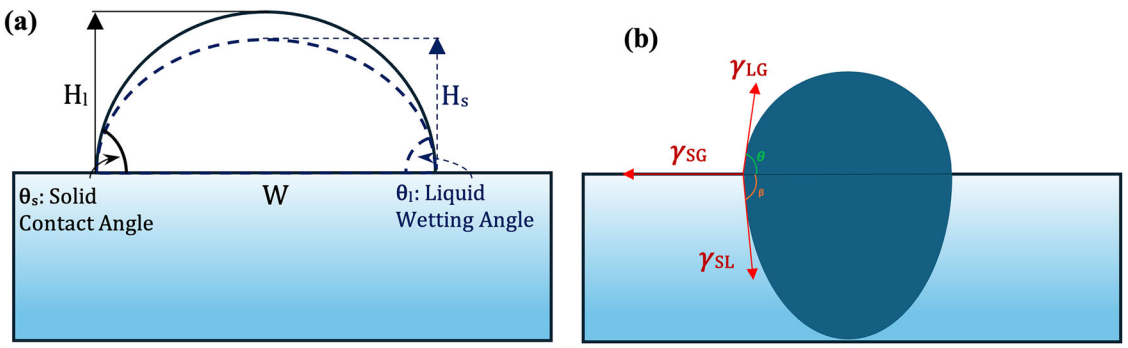


Fig. 3 | Liquid and solidified contact angles, heights, and interfacial-energy schematic. a Cross-sectional view of a melt droplet (dashed arc) and its solidified cap (solid arc) on a flat substrate: W is the track width; H_l and H_s are the liquid and solid heights; θ_l and θ_s are the corresponding liquid wetting and solid contact angles. **b** Vector diagram of the three interfacial tensions at the contact line: γ_{LG} (liquid–gas), γ_{SL} (solid–liquid) and γ_{SG} (solid–gas).

corresponding solid height via the following relationship:

$$2H_s \cot\left(\frac{\theta_s}{2}\right) = 2H_l \cot\left(\frac{\theta_l}{2}\right) \tag{33}$$

which simplifies to

$$H_l = H_s \left(\frac{\cot\left(\frac{\theta_s}{2}\right)}{\cot\left(\frac{\theta_l}{2}\right)}\right) \tag{34}$$

Here, θ_s and θ_l represent the contact angles of the solidified and liquid phases, respectively.

To estimate β, the melt pool geometry (depth D and width W) from Fig. 3 can be used:

$$\beta = \sqrt{2}\tan^{-1}\left(\frac{2D}{W}\right) \tag{35}$$

In addition, the solid and liquid arc length ratio can be calculated as follows:

$$\frac{S_l}{S_s} = \frac{R_l 2\theta_l}{R_s 2\theta_s} = \frac{\theta_l \frac{W}{2\sin(\theta_l)}}{\theta_s \frac{W}{2\sin(\theta_s)}} = \frac{\theta_l \sin(\theta_s)}{\theta_s \sin(\theta_l)} \tag{36}$$

Notably, the solid's curvature (κ) is greater than the liquid's.

Hatch spacing criteria

Hatch space criterion I: depth-height-width of single track and steady-state track. The track height and depth focus on the shape of the solidified material above the surface and the penetration area below. Above the surface, the shape aligns with a circle, whereas below, it approximates a parabola. Although the parabola does not perfectly fit the shape, it effectively predicts depth and provides other valuable relationships. Figure 4 illustrates this concept via two circles: one fitted over the track surface and another with a diameter equal to W and a parabola fitted over the depth of the melt pool.

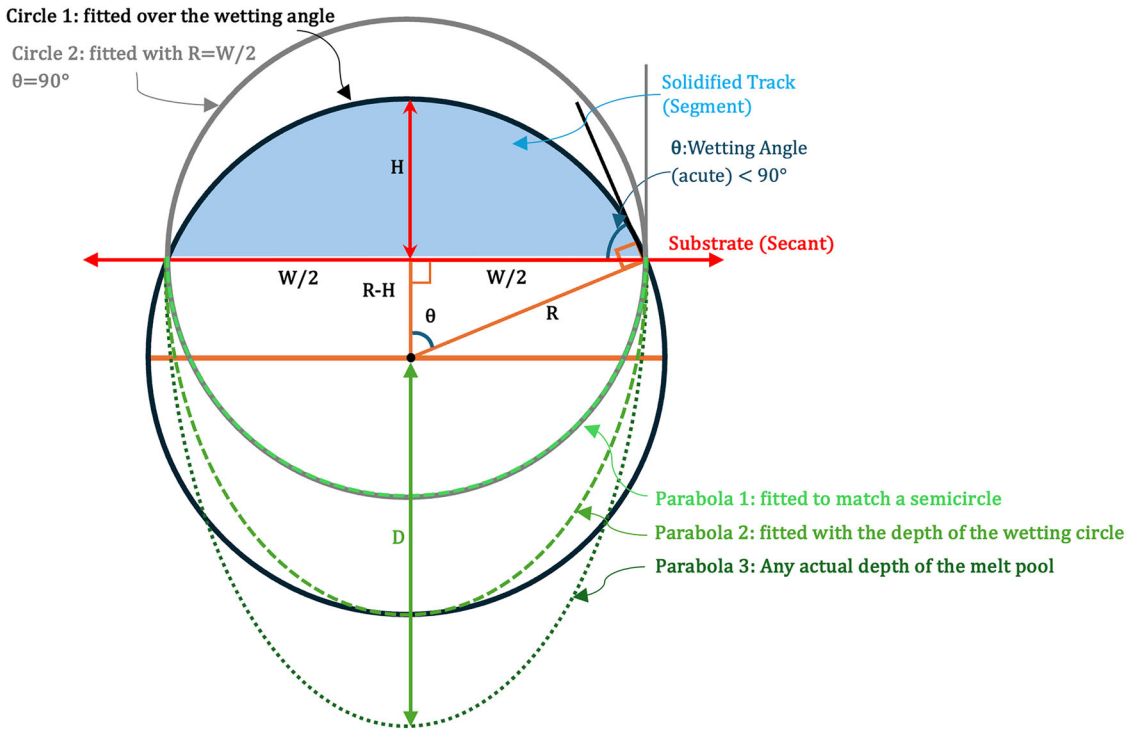


Fig. 4 | Illustration of the parabolas and circles fitted on the track.

The circular segment representing the track height for both acute and obtuse cases is shown in Fig. 4 and is described by the following equations:

$$(x)^2 + \left(y_c + (R - H)\right)^2 = R^2 \tag{37}$$

$$y_c = -\frac{W^2 - 4H^2}{8H} + \sqrt{\left(\frac{W^2 + 4H^2}{8H}\right)^2 - x^2} \tag{38}$$

$$y_c = -(R - H) + \sqrt{R^2 - x^2} = -R\cos\theta + \sqrt{R^2 - x^2} \tag{39}$$

These equations provide the fitting equation to determine the circle that fits the track reinforcement segment.

The full expansion of Eq. (37) gives

$$x^2 + y_c^2 + 2y_cR - 2y_cH - 2RH + R^2 + H^2 = R^2 \tag{40}$$

At point $(W/2, 0)$, the radius of track R can be determined as follows:

$$\frac{W^2}{4} - 2RH + H^2 = 0 \tag{41}$$

$$R = \frac{W^2 + 4H^2}{8H} \tag{42}$$

This result is consistent with Eq. (16), which is derived via a different approach. The agreement between these two equations suggests that the method used here leads to the same expression for the track radius, further validating the accuracy of the earlier derivation.

Continuing the geometric analysis, the following equations describe the parabolic shape of the track depth as shown in Fig. 4 :

$$y(x) = dx^2 - D \tag{43}$$

$$y_p = \frac{4D}{W^2}x^2 - D \tag{44}$$

By substituting Eqs. (2) and (10) into Eq. (45), we obtain:

$$y_p = \frac{D}{R^2\sin^2(\theta)}x^2 - D \tag{45}$$

Continuing the analysis, the maximum hatch spacing determines the overlap between successive tracks, which ensures proper fusion and minimizes the porosity in each layer. An analysis of the overlapping track geometry in Fig. 5, combined with previously derived equations, yields the relationship between the maximum hatch spacing and track dimensions based on the criteria provided by Zhang et al.[18].

We first consider the track height at a specific point to determine the maximum hatch spacing. Specifically, we examine the height at the point $(x = h/2, y_c = H')$:

$$\begin{aligned} H' = y_c &= -\frac{W}{2}\cot\theta + \sqrt{\left(\frac{W}{2\sin\theta}\right)^2 - \left(\frac{h}{2}\right)^2} \\ &= -R\cos\theta + \sqrt{R^2 - \left(\frac{h}{2}\right)^2} \end{aligned} \tag{46}$$

The difference between the circle and the parabola

$$\begin{aligned} y_c - y_p &= -R\cos\theta + \sqrt{R^2 - x^2} - \tfrac{D}{R^2\sin^2(\theta)}x^2 + D \\ &= -\tfrac{W^2 - 4H^2}{8H} + \sqrt{\left(\tfrac{W^2 + 4H^2}{8H}\right)^2 - x^2} - \tfrac{4D}{W^2}x^2 + D \end{aligned} \tag{47}$$

Under the assumption that the maximum hatch space is $H' + D' = H$ At $(x = h/2, y_c - y_p = H)$:

$$H = y_c - y_p = -R\cos\theta + \sqrt{(R)^2 - \left(\frac{h}{2}\right)^2} - \frac{D}{R^2\sin^2(\theta)}\left(\frac{h}{2}\right)^2 + D \tag{48}$$

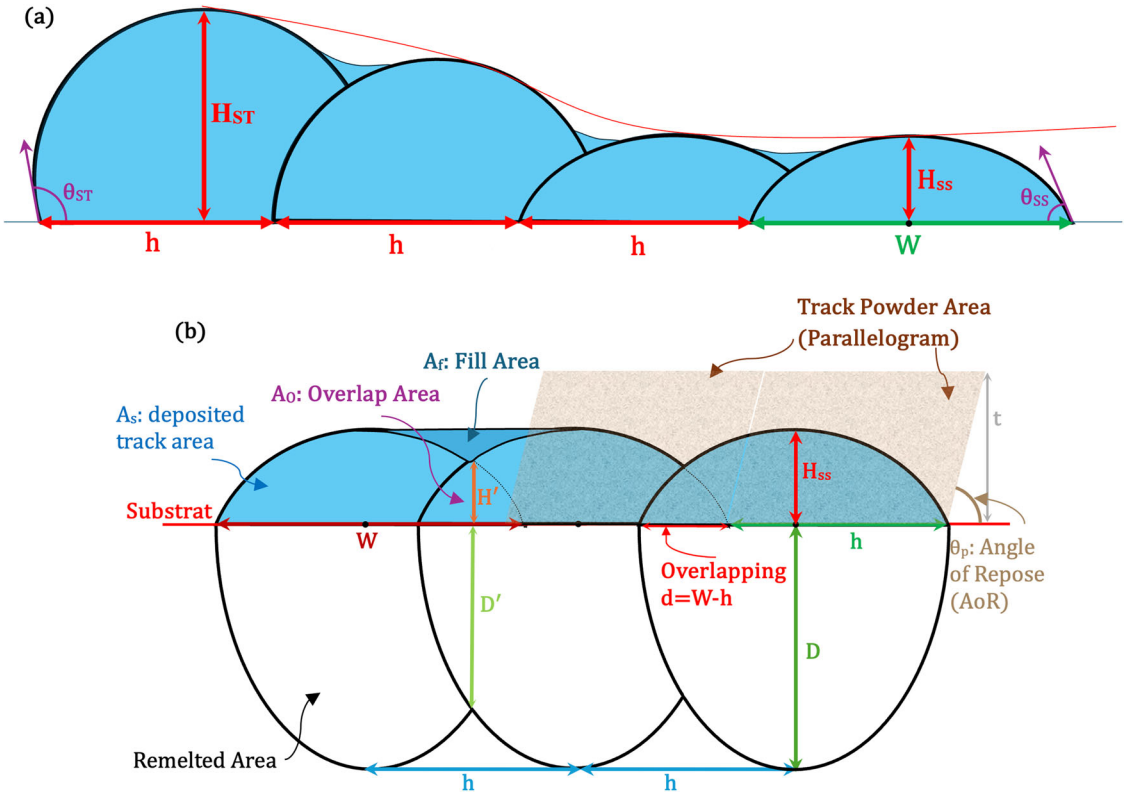


Fig. 5 | Melt-track evolution and steady-state overlap. a Cross-sectional profiles of successive melt tracks, the first track (left) converges to the steady-state (right). **b** Steady-state overlap (with a steady state powder layer grey parallelogram of thickness (t) at repose angle (θ_p): three adjacent tracks of width (W) separated by hatch spacing (h) produce an overlap distance ($d = W - h$).

At ($x = 0, y_c - y_p = H + D$):

$$H + D = y_c - y_p = R(1 - \cos\theta) + D \tag{49}$$

In Fig. 5, assuming that a line that passes through points D and D' intersects with another line passing through points H and H' on the substrate, the resulting triangles are similar, and the ratios of their corresponding sides are given as follows:

$$\frac{D'}{D} = \frac{H'}{H} \quad \text{or} \quad \frac{D'}{H'} = \frac{D}{H} \tag{50}$$

To ensure full penetration and avoid unmelted regions, it should be $D' + H' = H$. Therefore:

$$D' = D\frac{H'}{D' + H'} = D\frac{1}{\frac{D'}{H'} + 1} = D\frac{1}{\frac{D}{H} + 1} = \frac{HD}{H + D} \tag{51}$$

At the middle point of the overlap region from parabola Eq. (44) ($x = h/2, y_c = -D'$):

$$D' = D\left(1 - \frac{h^2}{W^2}\right) \tag{52}$$

Replacing D' from Eq. 51 yields:

$$\frac{HD}{H + D} = D\left(1 - \frac{h^2}{W^2}\right) \tag{53}$$

$$\frac{H}{H + D} = 1 - \frac{h^2}{W^2} \tag{54}$$

$$h^2 = W^2\left(1 - \frac{H}{H + D}\right) \tag{55}$$

$$h_{ST} = W\sqrt{\frac{D}{D + H}} \tag{56}$$

This model predicts the maximum hatch spacing based on a single track's dimensions. The hatch spacing is maintained as a fraction of the track width. In particular, as the depth and height converge (i.e., when $D = H$), the hatch spacing approaches ~0.71 W.

The height of a single track is always greater than that of steady-state tracks. Therefore, the model should rely on the height of a single track, not the steady-state height ($\rho_r t$), as it will predict a more accurate and optimal hatch spacing. The model predicts a larger hatch spacing when the depth increases. Similarly, if the height decreases due to a reduced powder layer thickness or reduction in AoR, the model also predicts greater hatch spacing.

When the system reaches the steady-state condition—ensuring complete remelting of the previous layer regardless of the specific overlap height H'—a substitution of $D' = H$ in Eq. (50) yields $H' = \frac{H^2}{D}$. Applying the same substitution in Eq. (52) reformulates Eq. (56) as

$$h_{SS} = W\sqrt{\frac{D - H}{D}}, \tag{57}$$

where W, D, and H represent the width, depth, and height of the steady-state track, respectively. This expression is then used to determine the maximum hatch spacing. Under steady-state conditions, to achieve $h = 0.71\ W$, it must be that $D = 2\ H$.

Hatch space criterion II: deposited track area of a steady-state track. The initial track printed on a powder bed differs from the subsequent

tracks as they reach a steady-state condition[6]. The first track, influenced by the powder bed characteristics, tends to be greater in height because of its trapezoidal cross-sectional powder area, which consumes more powder. However, as subsequent tracks are deposited with a defined hatch spacing, they progressively reach a steady state after a few tracks. In this state, the sharp overlapping regions shown in Fig. 5 between the tracks are characterized by smoother transitions, with the contact angle decreasing due to the preference of the new track to wet the previous track, minimizing surface energy through surface tension. Consequently, powder consumption in the steady state is based on the hatch space rather than the initial track width, forming a parallelogram area that effectively utilizes a lower powder volume to form the track. This shift results in a more consistent track profile, as depicted in Fig. 5.

The following equations describe the relationships between the track dimensions and powder volume for successive tracks in the steady state to find the maximum hatch space, as illustrated in Fig. 5.

In the single-track state, the volume of powder consumed by the initial solidified single track is calculated via the trapezoidal cross-sectional area of the powder bed, which is defined as follows:

$$V_{p(ST)} = A_{p(ST)}l = (\text{Trapezoid Area})l = (b + W)tl \tag{58}$$

where the cross-sectional solidified track area in the initial state A_i can be expressed as:

$$A_i = \varphi_{H(ST)}H^2_{(ST)} = \rho_r((b + W)t) \tag{59}$$

Once the process reaches a steady state, the volume of powder consumed by successive tracks changes to a parallelogram-shaped area:

$$V_{p(ss)} = A_{p(ss)}l = (\text{Parallelogram Area})l = htl \tag{60}$$

This shows that since $b + W$ (the base width plus the initial track width) is significantly larger than h (the hatch spacing), the initial track is much larger than the steady-state tracks are.

The cross-sectional area of the steady-state track can be calculated as follows:

$$A_s = \varphi_{H(ss)}H^2_{(ss)} = \rho_r th \tag{61}$$

The deposition rate (build rate) is then given by

$$\dot{D} = A_s \rho v \tag{62}$$

When the steady state condition is reached:

$$\rho_r t = H_{ss} \tag{63}$$

which indicates that the product of the relative density of the powder (ρ_r) and the effective layer thickness ($t_{\text{eff}} = t = \frac{t_i}{\rho_r}$) equals the steady-state track height (H_{ss}) during the printing of each layer after printing a few layers. In practical terms, this means that if the machine is set to use an initial powder layer thickness t_i (for example, 40 μm), then after the layer has been printed, the final solidified height of each layer will also be 40 μm, that is, $H_{ss} = t_i$.

This relationship arises because the printing process is pre-engineered to meet specific dimensional requirements. The machine is designed such that the thickness of the final, solidified structure matches the predetermined value. In a multilayer build, the total height is simply the number of layers (n) multiplied by the initial layer thickness (i.e., $H_{\text{total}} = n\, t_i = n\, H_{ss}$), ensuring that the final printed object has the desired dimensional integrity.

Therefore, the hatch spacing can be determined via the steady state track height and height wetting shape factor, as given by:

$$h_\varphi = \frac{A_s}{H_{ss}} = \varphi_H H \tag{64}$$

This approach predicts the optimal hatch spacing on the basis of only steady-state track attributes, irrespective of depth variations. Once the steady-state track height is determined and the contact angle is known, the corresponding hatch spacing can be readily calculated. In practice, the model typically yields a hatch spacing of ~0.71 ($\frac{1}{\sqrt{2}} = \cos 45^\circ$) times the track width, implying that setting the maximum hatch spacing to 0.71 times the width is crucial for achieving complete penetration and a fully dense printed part. In summary, Eqs. (56), (57), and (64) provide a comprehensive framework for predicting the maximum hatch spacing by integrating parameters derived from both single-track and steady-state analyses.

Hatch space criterion III: overlap and gap filling areas between steady-state tracks. The overlap area of successive tracks denoted as A_o (Fig. 5), is determined by considering the geometry of the track's cross—section. The A_o can be expressed as

$$\begin{aligned} A_o =& 2\int_{h/2}^{W/2}\left(-R\cos\theta + \sqrt{R^2 - x^2}\right)dx \\ =& -R\cos\theta\,(W - h) + \frac{W}{2}\sqrt{R^2 - \frac{W^2}{4}} + R^2\arcsin\left(\frac{W}{2R}\right) \\ & -\frac{h}{2}\sqrt{R^2 - \frac{h^2}{4}} - R^2\arcsin\left(\frac{h}{2R}\right) \end{aligned} \tag{65}$$

In parallel, the valley or gap area between successive tracks is denoted by A_f. This area accounts for the nominal rectangular region, defined by the product Hh, minus the portion accounted for by the same circle integration over the range from 0 to $\frac{h}{2}$. Mathematically, this gap area is calculated as

$$\begin{aligned} A_f &= Hh - 2\int_0^{h/2}\left(-R\cos\theta + \sqrt{R^2 - x^2}\right)dx \\ &= Hh + Rh\cos\theta - \frac{h}{2}\sqrt{R^2 - \frac{h^2}{4}} - R^2\arcsin\left(\frac{h}{2R}\right) \end{aligned} \tag{66}$$

To ensure a continuous and minimum surface roughness, it is essential that the remelted top portion from the previous track, represented by the area A_o, perfectly fills the gap denoted by A_f between successive tracks. Imposing the condition $A_o = A_f$, and solving for the parameter h yields

$$h_o = \frac{-RW\cos\theta + \frac{W}{2}\sqrt{R^2 - \frac{W^2}{4}} + R^2\arcsin\left(\frac{W}{2R}\right)}{H} \tag{67}$$

In this equation, the numerator represents the area of the deposited portion of the track. This area is obtained by integrating Eq. (39) from $-W/2$ to $W/2$, which yields the same expression as Eq. (64), namely $\frac{A_{ss}}{H_{ss}} = \varphi_H H$. This derived hatch spacing relationship delineates the essential conditions for producing a fully dense layer. By satisfying this criterion, the process avoids surface irregularities—eliminating both protrusions and depressions—to achieve a uniformly smooth surface.

Absorption and normalized enthalpy

The concept of NE was initially introduced in autogeneous laser welding by Hann et al.[13] and later adapted for AM by King et al.[15]. In this section, a scaled version of the NE is derived, and its correlation with the normalized melt pool depth is investigated to determine an effective

absorption coefficient. This coefficient is subsequently employed to calibrate the NE, accurately representing the process energy absorption characteristics. Furthermore, NE is compared with key energy metrics—volumetric energy density (VED) and normalized volumetric energy density (NVED)—to elucidate their interrelationships and to capture the energy delivered to the material, thereby evaluating the effectiveness of each metric.

The laser intensity (I), representing the power per unit area, which characterizes how the power is distributed over the beam spot, is given by

$$I = \frac{P}{A_0} \tag{68}$$

where P is the laser power and A_0 is the area of the laser spot on the surface. For both flat-top and Gaussian beam profiles, the spot area is given by

$$A_0 = \pi\omega_0^2, \tag{69}$$

When the interaction time is considered, the laser's power can be converted into fluence—defined as the energy delivered per unit area. The laser surface energy density (fluence) is defined as in ref. 19

$$F = \frac{E}{A_0}, \tag{70}$$

where the laser energy is given by

$$E = P\,t_{\text{int}} \tag{71}$$

and t_{int} is the interaction time, which is defined as

$$t_{\text{int}} = \frac{2\omega_0}{v} \tag{72}$$

where v is the laser scan speed and ω_0 is the beam radius. The peak fluence for a Gaussian beam is twice the average fluence[20], i.e.,

$$F_{\text{peak}} = 2F = \frac{2E}{\pi\omega_0^2} \tag{73}$$

The average fluence or surface energy density should be divided by the thermal diffusion length (L) to obtain the volumetric absorbed energy density. ΔH is the change in volumetric enthalpy relative to a reference point. When the pressure-volume work is negligible, or when the process occurs under approximately constant pressure conditions, ΔH can be interpreted as the change in energy per unit volume. The absorbed volumetric enthalpy density (VHD) (i.e., the enthalpy per unit volume) is

$$\text{Volumetric Enthalpy Density} = \Delta H = \frac{\eta F}{L} = \frac{\eta E}{A_0\,L} = \frac{\eta E}{\pi\omega_0^2\,L} = \frac{\eta P t_{int}}{\pi\omega_0^2\,L} \tag{74}$$

which shows how the absorbed energy (via η as the absorption coefficient and the laser power P and interaction time t_{int}) is distributed over the laser spot (area $\pi\omega_0^2$) and scaled by the thermal diffusion length L. Alternatively, if the denominator is reformulated to incorporate the hatch spacing (h) and the layer (or powder) thickness (t)—that is, replacing $\pi\omega_0^2\,L$ with $2\omega_0\,h\,t$—the expression becomes the VED:

$$\text{Volumetric Energy Density} = \frac{\eta P t_{int}}{2\omega_0\,h\,t} = \frac{\eta P}{v h\,t} \tag{75}$$

The Fourier heat conduction equation can be applied to determine L. In a homogeneous medium with no internal heat sources, the Fourier law of the heat conduction equation[21]

$$\frac{\partial T}{\partial t} = \alpha\nabla^2 T \tag{76}$$

holds where $T = T(x, t)$ is the temperature, ∇^2 is the Laplacian operator (spatial second-order derivative), and α is the thermal diffusivity. By applying dimensional analysis $\frac{\partial T}{\partial t} \sim \frac{T}{t}$ and $\nabla^2 T \sim \frac{T}{L^2}$, we obtain $\frac{T}{t} \sim \alpha\frac{T}{L^2}$ and hence $L^2 \sim \alpha t$.

$$L = \sqrt{\alpha\,t_{\text{int}}} \tag{77}$$

where L represents the thermal diffusion length—the distance over which a temperature disturbance significantly diffuses in time t_{int}.

The thermal diffusivity, α, is defined as

$$\alpha = \frac{k}{\rho c_p} \tag{78}$$

where k being the thermal conductivity, ρ is the density, and c_p is the specific heat capacity (evaluated at the liquidus). By substituting L in place of $\sqrt{\alpha\,t_{\text{int}}}$, Eq. 74 becomes

$$\Delta H = \frac{\eta P\,t_{\text{int}}}{\pi\omega_0^2\sqrt{\alpha\,t_{\text{int}}}} \tag{79}$$

Substituting $t_{\text{int}} = \frac{2\omega_0}{v}$ for Gaussian and flat-top beam profiles into the above expression yields

$$\Delta H = \frac{\sqrt{2}\,\eta P}{\pi\sqrt{\alpha\,v\omega_0^3}} \tag{80}$$

This expression for ΔH (VHD) offers a more realistic measure of energy deposition. Unlike traditional VED, which depends on hatch spacing and powder layer thickness and is inversely proportional to the laser speed, this formulation integrates the laser spot properties, resultant fluence, and thermal diffusion length, leading to a square-root dependency on speed. This improved scaling reflects effective heat diffusion during processing, making it a more practical and reliable metric for laser-material interactions.

To achieve normalized VHD or NE, the volumetric enthalpy should be divided by the volumetric enthalpy at melting (h_s), yielding the expression

$$NE = \frac{\Delta H}{h_s} = \frac{\sqrt{2}\,\eta P}{h_s\pi\sqrt{\alpha\,v\omega_0^3}} \tag{81}$$

The volumetric enthalpy required to heat a material from a build plate preheat temperature T_{preheat} to complete melting (sensible and latent), h_s, is given by ref. 22

$$h_s = \Delta h_{\text{preheat}\to\text{liquidus}} = \int_{\text{preheat}}^{T_{liquidus}} \rho(T)\,c_p^{\text{solid}}(T)\,dT + \rho(T_m)\,L_m \tag{82}$$

Under the assumption of constant density ρ and constant specific heat c_p, the expression simplifies to

$$h_s = \Delta h_{\text{preheat}\to\text{liqudus}} = \rho\,c_{p,s}\,(T_{liquidus} - T_{\text{preheat}}) + \rho\,L_m \tag{83}$$

Similarly, by dividing the classic VED, Eq. (71), by the enthalpy at melting, we obtain the normalized VED (NVED) expressed as

$$\text{NVED} = \frac{\Delta H}{h_s} = \frac{\eta P}{h_s\,h\,v\,t} \tag{84}$$

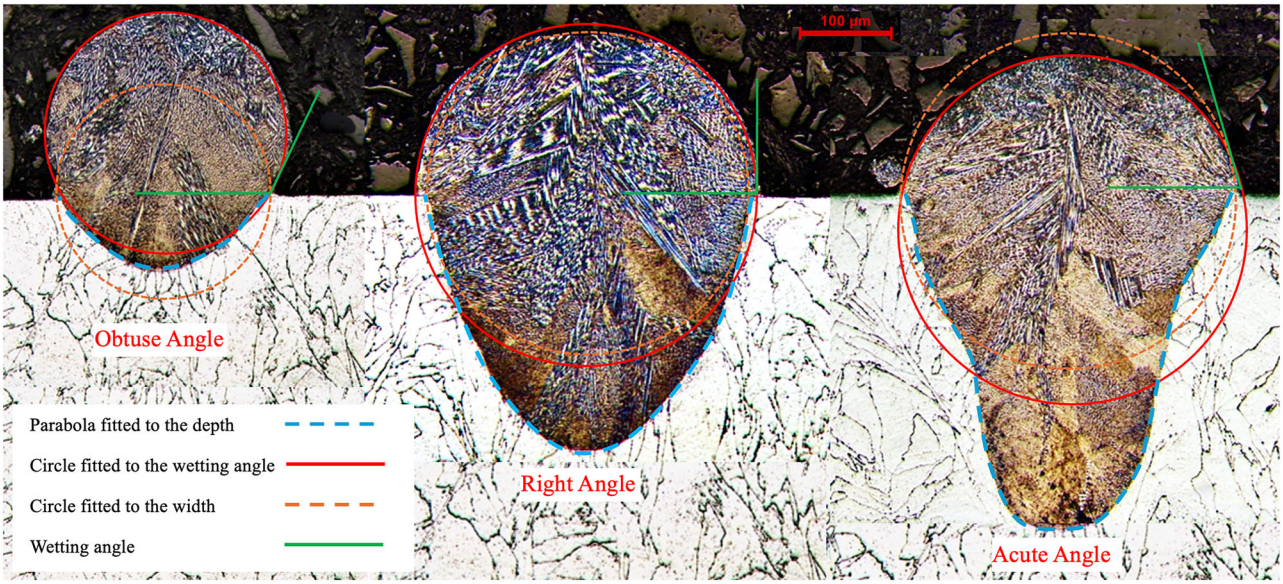


Fig. 6 | Fitted circles, wetting angles, and parabolas for acute and obtuse angles with a powder layer thickness of 130 µm.

Dimensionless energy density contextualizes the energy input relative to the melting energy, providing a standardized framework for assessing energy efficiency in various thermal processes.

Importantly this model was developed for conditions with zero powder layer thickness (i.e., autogenous welding or laser processing on a bare substrate). In contrast, when adapting the model to AM processes—whether a powder bed, powder feed, or wire feed—the required NE must be greater to achieve the same penetration depth as in autogenous processing.

However, absorption is a critical parameter that influences the actual NE, varies with process conditions, and is challenging to measure indirectly. The effective absorption (the absorption of the laser within the substrate) values can be determined by correlating the NE with the keyhole number and the square root of the dimensionless depth:

$$NE = \Phi\sqrt{\delta^*} \tag{85}$$

where δ^* represents the normalized dimensionless depth, which is defined as the ratio of the melt pool depth to its half-width:

$$\delta^* = \frac{2D}{W} \tag{86}$$

Φ denotes the threshold between the conduction and keyhole modes, known as the keyhole number. The keyhole number Φ is defined as the ratio of the vaporization enthalpy to the melting enthalpy:

$$\Phi = \frac{h_v}{h_s} \tag{87}$$

Here, h_s represents the specific enthalpy (either mass- or molar-based) required to heat the material at 1 atm from the standard reference temperature T_{ref}=298.15 K to the liquidus temperature—thereby completing melting through both sensible and latent heat contributions—while h_v denotes the specific enthalpy necessary to further heat the material from the reference state through melting and up to complete vaporization.

The specific enthalpy for complete melting (liquidus) is given by

$$h_s = \Delta h_{\text{ref}\to\text{liquidus}} = \int_{T_{\text{ref}}}^{T_{liquidus}} c_p^{\text{solid}}(T)\,dT + L_m \tag{88}$$

where $c_p^{\text{solid}}(T)$ is the temperature-dependent specific heat of the solid and where L_m is the specific latent heat of melting. Under the assumption of a constant specific heat $c_{p,s}$, this expression simplifies to

$$h_s = \Delta h_{\text{ref}\to\text{liquidus}} = c_{p,s}\,(T_{liquidus} - T_{\text{ref}}) + L_m \tag{89}$$

Similarly, the specific enthalpy required for complete vaporization is expressed as

$$h_v = \Delta h_{\text{ref}\to\text{completevaporization}} = h_s + \int_{T_m}^{T_{vap}} c_p^{\text{liquid}}(T)\,dT + L_v \tag{90}$$

The integral accounts for the sensible heating of the liquid from the melting temperature T_m to the vaporization temperature T_{vap}, and L_v is the specific latent heat of vaporization. With the assumption of a constant liquid specific heat $c_{p,\ell}$, this expression further reduces to

$$h_v = \Delta h_{\text{ref}\to\text{completevaporization}} = h_s + c_{p,\ell}\,(T_{vap} - T_m) + L_v \tag{91}$$

The Φ values are 13.1 for pure aluminum (AA1000), 12.45 for AL-10Si-Mg, 8.6 for Inconel 625, 8.45 for Inconel 738LC, 7.95 for Inconel 718, 8.22 for Inconel 939, 7.6 for Ti-6Al-4V, 9 for pure copper (C11000), 7.4 for SS316L, and 7.94 for CoCrMo, as determined via Thermo-Calc 2025a[23]. When the NE exceeds this ratio, the process typically transitions into keyhole mode. Additionally, the NE behaves analogously to the Stefan number (the ratio of sensible heat to latent heat), and for conditions in which the Fourier number is less than 1, it predicts changes in the melt pool depth provided that the Biot number is sufficiently large.

To determine the energy absorptivity of the substrate, Eq. (85) is rearranged to yield the effective absorptivity

$$\eta = \frac{\Phi\sqrt{\delta^*}}{NE_{\eta=1}} \tag{92}$$

Additionally, the absorption coefficient is given as follows when $NE_{\eta=1}$ is substituted into the above equation:

$$\eta = \frac{\Phi\pi\, h_s \sqrt{\delta^*\,\alpha\,\nu\,\omega_0^3}}{\sqrt{2}\,P} \tag{93}$$

The absorption values calculated via δ^* are subsequently used to calibrate *NE*. Notably, this equation does not imply that increasing the power necessarily reduces the absorptivity, as δ^* also increases. Ultimately, the effective absorptivity depends on the interplay among all the variables.

Results and discussion

Wetting angle, width, and height

Figure 6 illustrates the different modes of melt tracks in IN625, categorized by their corresponding wetting angles: obtuse, right, and acute. These modes were produced using powder layer thicknesses of 130 μm, various laser powers, and laser scanning speeds. The attributes of the upper surface of the tracks can be determined via the provided equations by relating specific parameters.

The left side of Fig. 6 displays the conduction mode with an obtuse wetting angle of 117.5° (depicted by the green line, calculated via Eq. (15). In this mode, the radius of the wetting angle circle (indicated by the red line) is 130 μm (calculated via Eq. 16), which is larger than the half-width radius of 112.5 μm (represented by the dashed orange line, which always has a right angle at the surface). The height of the melt track in this mode is 195 μm, substantially exceeding its depth of 75 μm (shown by the dashed blue line).

Conversely, the keyhole mode is distinguished by an acute wetting angle of 78.5°. In this mode, the radius of the circle corresponding to the wetting angle is 184 μm, which is larger than the radius of the half-width circle at 175 μm. The depth of the track in keyhole mode reaches 345 μm, significantly surpassing both the half-width and the wetting angle circle radius.

The red and dashed orange lines in the right-angle scenario appear almost identical in radius despite a slight visual difference. In reality, their radii are nearly the same. For a wetting angle of 90°, the properties of the melt track can be determined via equations applicable to acute and obtuse cases. In this mode, the radius of the width circle (half-width) and the radius of the wetting angle circle (corresponding to the height) are 170 μm. The track depth, 250 μm, typically exceeds the half-width value. This analysis demonstrated that transitioning from balling to conduction and keyhole modes decreases the wetting angle. This decrease is attributed primarily to the increase in melt pool width and the concurrent reduction in height. In both conduction mode and keyhole mode, the diameter of the circle fitted to the melt track width is consistently smaller than that of the circle fitted to the wetting angle. A significant morphological change occurs beneath the surface, where the shape of the melt pool transitions from circular to parabolic, signifying a shift from conduction mode to keyhole mode. Typically, this transition point coincides with the depth where the width-fitted circle intersects the melt pool.

Track area calculation using dimensionless shape factors

The area of the melt tracks can be determined via any of the height, radius, or width dimensionless wetting shape factors. The width shape factors for the tracks illustrated in Fig. 6, which are based on Eq. 23, are 0.78 for the 117.5° conduction mode, 0.39 for the 90° keyhole mode, and 0.30 for the 78.5° keyhole mode. By incorporating these width values and their respective dimensionless shape factors into Eq. (25), the calculated solidified areas are 38,200 μm^2 for the 117.5° track, 44,700 μm^2 for the 90° track, and 37,200 μm^2 for the 78.5° keyhole track. This analysis revealed that maintaining a constant track width and decreasing the contact angle reduced the solidified area of the track. The solidified area can also be calculated via the height or radius shape factor.

Powder layer thickness with respect to width and height

Mass conservation principles were applied to measure and relate the height or width of the melt track to the powder layer thickness and contact angle, and the effects of spatters, the denudation zone, and entrainment were assumed to be negligible. This allows for the calculation and correlation of the width and height of the track to the powder layer thickness. The quadratic equations for various contact angles and corresponding dimensionless width shape factors were calculated and are presented in Table 2. At many contact angles, the height of a single track is greater than the powder layer thickness. This is because, after the width of the track is determined by the laser power and scanning speed characteristics, the powder contribution to the formation of the first track is greater than that of the subsequent tracks. As shown in Table 2, for IN625 powder, with a powder relative density of 0.56 and an AoR of 30°, it is evident that, at certain wetting angles, the width and height and the width and powder layer thickness of the initial single track can become equal. For example, at an angle of 141°, the width of a track is equal to its height in a single-track scenario. The height of the initial single track is consistently greater than the powder layer thickness, as demonstrated in Fig. 8. Additionally, reducing powder consumption corresponding to the formation of a track in successive tracks causes the layer height to fall below the effective powder layer thickness, leading to a steady state track height equal to the initial powder layer thickness.

Equations (28) and (30) have also been validated under real printing conditions. The effective powder layer thickness, *t*, was calculated for various single tracks printed on top of a 100—layer built part. An initial powder layer thickness of 40 μm was employed along with a relative density, $\rho_r = 0.55$, and an AoR, $\theta = 30°$. The track width and contact angle were obtained via cross-sectional analysis, and *t* was subsequently determined via Eqs. (28) and (30). The results in Supplementary Table S2 show that the predicted average steady-state powder layer thickness, given by $t_{\text{effective}} = \frac{t_{\text{initial}}}{\rho_r} = \frac{40}{0.55} \approx 72.7\mu\text{m}$, is ~72.97 μm, thereby confirming the accurate predictive capability of the applied equations.

Depth and normalized enthalpy

Figure 7 illustrates six distinct tracks that reveal the relationship between NE and dimensionless depth for the alloys IN65, IN738LC, Al10SiMg, and AA1000. The detailed data for these tracks are summarized in Table 3.

Figure 7a, b illustrate the melt pool cross-section of the IN625 alloy, which has a keyhole number of $\Phi = \frac{h_v}{h_s} = 8.6$. Tracks (a) and (b) depict deep and shallow keyholes, with absorptivity values of 0.74 and 0.70 and calibrated NE values of 14.88 and 10.32, respectively. Although the absorptivity in both cases is ~0.7, the deep keyhole shows a greater decrease in NE ($20.24 - 14.88 = 5.36$) than does the shallow keyhole ($14.74 - 10.32 = 4.42$). This difference is primarily due to increased energy absorption by the powder above the substrate; for instance, the powder area

Table 2 | Quadratic equations, and the related values of *W*, *H*, and *t* for the initial single track of IN625 powder, with a powder relative density of 0.55 and an angle of repose of 30°

θ (°)	Quadratic equation (28, 30)	φ	x in $W = xH$	y in $W = yt$	z in $H = zt$
45	$0.25W^2 - Wt - 1.73t^2 = 0$	0.14	3.83	5.34	1.4
60	$0.37W^2 - Wt - 1.73t^2 = 0$	0.21	3.46	3.90	1.13
90	$0.70W^2 - Wt - 1.73t^2 = 0$	0.39	2.00	2.44	1.22
122.5	$1.60W^2 - 1.19Wt - 1.73t^2 = 0$	0.90	1.10	1.48	1.34
125.4	$1.79W^2 - 1.23Wt - 1.73t^2 = 0$	1.00	1.03	1.39	1.35
126.9	$1.86W^2 - 1.25Wt - 1.73t^2 = 0$	1.04	1.00	1.36	1.36
141	$3.18W^2 - 1.6Wt - 1.73t^2 = 0$	1.78	0.71	1.00	1.41

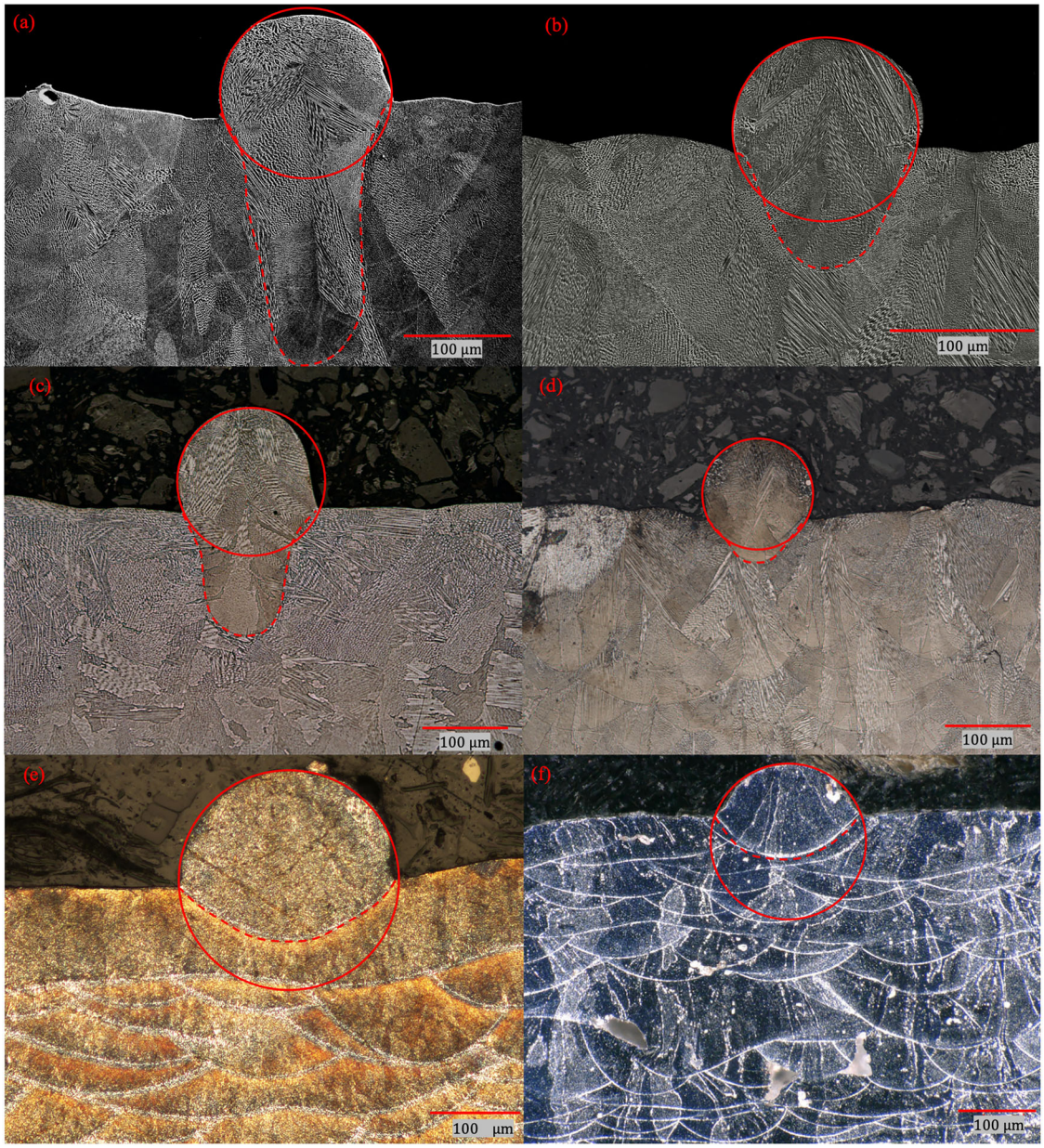


Fig. 7 | Cross-sectional views of the tracks used to calculate $NE_{\eta=1}$, absorption η, and calibrated NE. The corresponding track data are listed in Table 3: **a**, **b** IN625, **c**, **d** IN738LC, **e** Al10SiMg, and **f** AA1000.

for the deep keyhole is $A_s = 12{,}000\ \mu m^2$ compared with $A_s = 8500\ \mu m^2$ for the shallow keyhole. The powder layer thickness is greater (71 µm versus 64 µm). Consequently, more energy is consumed in melting the powder above the substrate, resulting in less energy reaching the substrate, while a higher NE also contributes to increased keyhole width and depth.

Figure 7c, d present the melt pool cross-sections of the IN738LC alloy with a keyhole number of $\Phi = 8.45$. Track (c) is produced in keyhole mode, whereas track (d) is generated in conduction mode. The absorption coefficients are 0.62 for track (c) and 0.58 for track (d). Additionally, the cross-sectional reinforcement area A_s is significantly larger for track (c) ($A_s = 18{,}000\ \mu m^2$) than for track (d) ($A_s = 10{,}500\ \mu m^2$). The powder layer thickness is greater for track (d), calculating 95 µm as opposed to 73 µm for track (c). Although the absorption is only marginally greater in keyhole mode by 0.04, the decrease in NE is more pronounced, with values of 7.06 for track (c) and 5.85 for track (d). This calibrated NE corresponds to the energy absorbed by the substrate since part of the input energy is used to melt the powder and form a reinforcement segment above the substrate, whereas additional losses occur through reflection, conduction, spatter, and plume dissipation. These effects are reflected in the track depth.

Tracks (e) and (f) in Fig. 7 present cross-sectional images of the AL10SiMg and AA1000 alloys processed in conduction mode, with corresponding keyhole numbers of $\Phi = 12.45$ and $\Phi = 13.1$, respectively. These greater keyhole numbers indicate that the difference between the enthalpies at evaporation and melting is more pronounced for aluminum alloys. This finding indicates that achieving keyhole mode in aluminum alloys requires a substantially higher energy input than in nickel-based alloys. In addition, these alloys' lower absorptivity, higher reflectivity, and increased thermal diffusivity hinder keyhole formation further. Under perfect absorption, the NE $NE_{\eta=1}$ is ~21 for both tracks. However, when an absorptivity of ~0.44 is considered, the NE decreases by nearly 12 units to ~9. This significant reduction underscores the importance of accounting for effective absorption conditions when evaluating the calibrated NE. Moreover, although the powder layer thickness is less than that of IN738LC and IN625, the absorption of these alloys is less than that of IN625 and 738LC, which

Table 3 | Process parameters and key attributes for tracks a–f in Fig. 7

Parameter	Unit	Track a	Track b	Track c	Track d	Track e	Track f
Material	–	IN625	IN625	IN738LC	IN738LC	Al10SiMg	AA1000
P	W	250	285	250	285	250	250
v	mm/s	400	980	442	1021	1600	1600
t	μm	71	64	95	73	30	54
H	μm	90	80	124	96	78	64
W	μm	165	125	160	115	177	179
D	μm	246	90	148	52	40	50
R	μm	83	40	88	48	89	95
θ	°	95	104	114	118	83	71
φ	–	0.44	0.54	0.71	0.79	0.34	0.26
A_s	μm^2	12000	8500	18000	10500	10500	8300
$NE_{\eta=1}$	–	20.24	14.74	18.57	13.93	20.63	21.19
NE	–	14.88	10.32	11.51	8.08	8.78	9.34
η	–	0.74	0.70	0.62	0.58	0.43	0.44
$\sqrt{\delta^*}$	–	1.73	1.20	1.36	0.95	0.67	0.75
Φ	–	8.6	8.60	8.45	8.45	12.45	13.1

further influences the total absorbed energy. Additionally, the width of aluminum alloys is wider than that of Inconel alloys because aluminum alloys are ~180 μm.

Tracks (e) and (f) in Fig. 7 show cross-sectional images of the AL10SiMg and AA1000 alloys processed in conduction mode, with corresponding keyhole numbers of Φ = 12.45 and Φ = 13.1, respectively. These high keyhole numbers reveal that the difference between the enthalpy at evaporation and melting is more pronounced in aluminum alloys. Consequently, achieving a keyhole mode in these alloys demands a substantially higher relative energy input than nickel-based alloys do. In addition, the lower absorptivity, higher reflectivity, and increased thermal diffusivity of aluminum alloys further hinder keyhole formation. Under perfect absorption, the NE $NE_{\eta=1}$ is ~21 for both tracks. However, when an absorptivity of ~0.44 is considered, the NE decreases by nearly 12 units to ~9. This marked reduction underscores the importance of accounting for effective absorption conditions when evaluating the calibrated NE. Moreover, although the powder layer thickness for aluminum alloys is lower than that used for IN738LC and IN625, their lower absorptivity additionally impacts the total absorbed energy. Finally, the track width for aluminum alloys is ~180 μm, which exceeds that of Inconel alloys.

Hatch spacing and steady-state tracks

Figure 8 illustrates the effect of using two different powder layer thicknesses and two different NEs, all processed with a 120 μm laser spot size. These variations help validate the predicted hatch spacing and demonstrate how the melt track achieves a steady state after several adjacent tracks are printed.

In Fig. 8a, the process parameters are set with an NE of 6.81, an absorption coefficient of 0.62, initial powder layer thicknesses of 35 μm, a steady state powder layer thickness of 63 μm, and a hatch spacing of 110 μm. Under these conditions, the single-track height is ~75 μm, whereas the steady-state track height is ~35 μm. The wetting angle decreases from 86° to 47°. After four adjacent tracks are printed, the track transitions from a single-track in conduction mode to a steady-state track in keyhole mode. During this transition, the powder cross-sectional profile changes—from a trapezoidal shape on a single track to a parallelogram shape on steady-state tracks. Consequently, less powder is available to absorb the laser energy, allowing more beam energy to penetrate deeper into the substrate. This deeper penetration and localized heat accumulation increase the build plate temperature. In addition, the reduced volumetric enthalpy of melting allows the substrate to absorb even more energy, further promoting the shift to keyhole-mode melting. Furthermore, the effective doubling of the peak fluence of the Gaussian laser beam—due to the melt pool depression zone trapping more photons—leads to additional absorption[24]. As a result, the NE increases from 6.81 to 8.81 while maintaining a constant laser power and scanning speed. Since the keyhole threshold for IN738LC is ~8.45, exceeding this value triggers keyhole-mode melting.

Three proposed Eqs. (56, 57, and 64) were used to calculate the maximum hatch spacing based on the single track and steady-state track attributes, predicting a maximum allowable range from ~110 to 135 μm. As shown in the figure, smooth transitions between adjacent tracks are observed with a hatch spacing of 110 μm, indicating that the selected hatch spacing is appropriate.

In Fig. 8b, the process parameters include an NE of 8.02, an absorption coefficient of 0.62, an initial powder layer thickness of 40 μm, a steady-state powder layer thickness of 71 μm, and a hatch spacing of 150 μm. Under these conditions, the single-track height is ~90 μm, whereas the steady-state track height is ~40 μm. The wetting angle decreases from 104° to 59°.

As five adjacent tracks are deposited, the melt pool transitions from conduction—mode melting in the initial single track to keyhole—mode melting in the steady-state tracks. During this progression, the absorption coefficient increases to 0.67, and the NE increases from 8.02 to 8.70, even though the laser power and scanning speed remain constant. Surpassing the keyhole number threshold of 8.45 confirms the onset of keyhole-mode melting. A maximum hatch spacing ranging from 100 to 108 μm was determined; in contrast, a hatch spacing of 150 μm is excessive, resulting in insufficient overlap between melt pools. As shown in Fig. 8, variations in track height, powder layer thickness, and wetting angle illustrate the evolution of these attributes during the transition from conduction mode to keyhole mode.

Liquid state track properties

To illustrate the changes in the wetting angle between the liquid and solid phases and the variation in track height, refer to Fig. 9. First, the Young-Laplace equation explains the convex shape of the melt pool. The positive pressure difference between the liquid and the atmospheric pressure results in a higher internal pressure within the liquid, resulting in a convex shape:

$$\Delta P = \gamma_{LG}\left(\frac{1}{R_1}+\frac{1}{R_2}\right) = \gamma\left(\frac{1}{R}\right) = \frac{1.7}{190\times10^{-6}} \approx 0.009\ \text{MPa} \qquad (94)$$

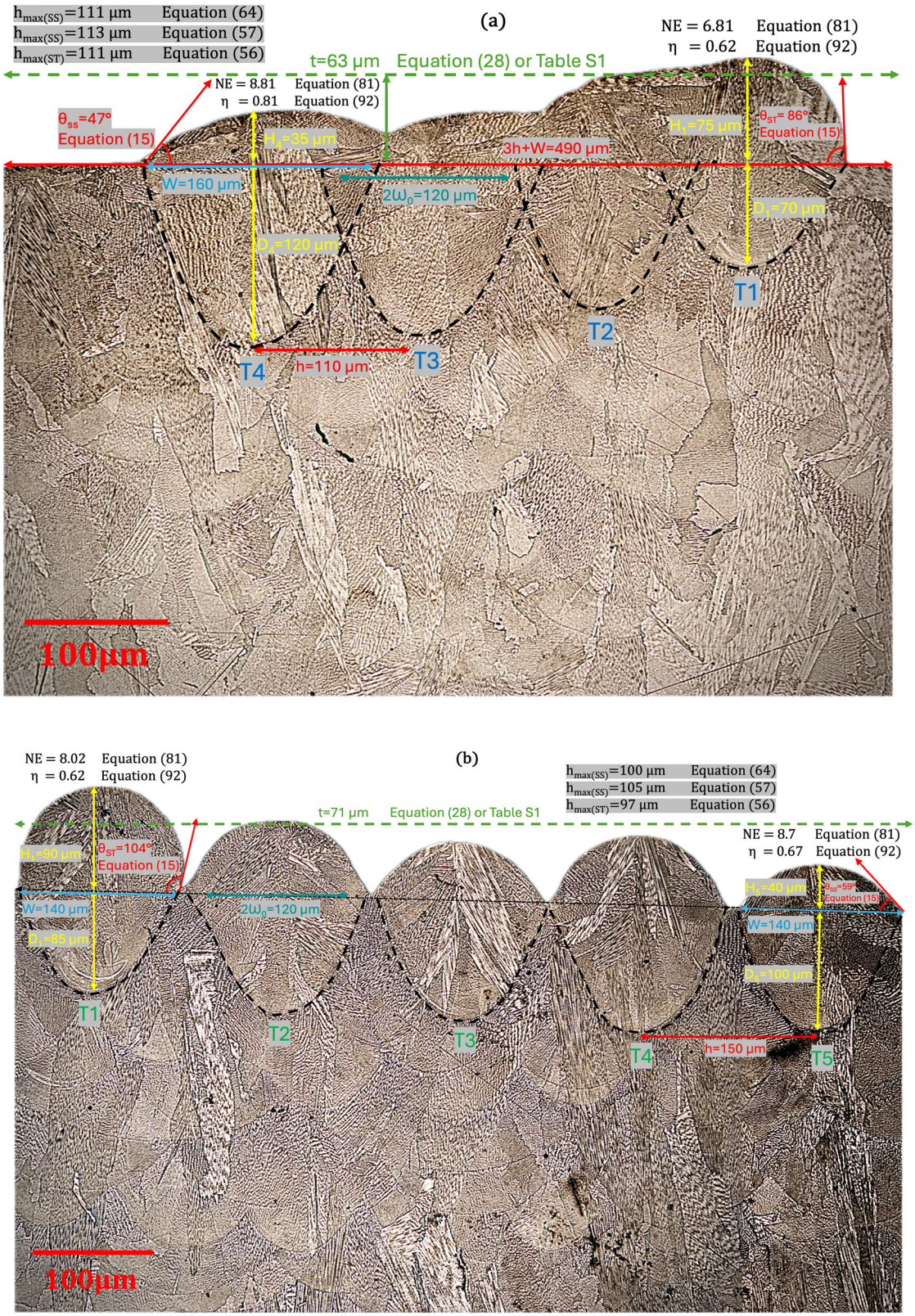


Fig. 8 | Illustration of the IN738LC track geometry evolving from conduction mode to keyhole mode when reaching the steady state condition. a Proper hatch spacing, **b** Excessive hatch spacing.

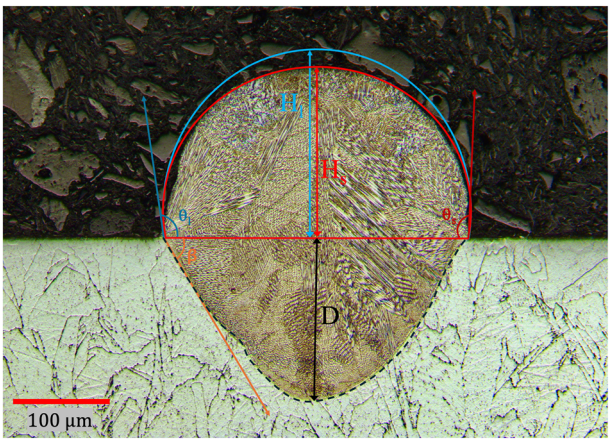


Fig. 9 | Illustration of the wetting angle and track height variation during solidification.

Next, to assess the significance of the gravitational forces, the Bd is calculated as follows:

$$Bd = \frac{\Delta\rho g R^2}{\gamma} = \frac{887 \times 9.8 \times (164 \times 10^{-6})^2}{1.7} = 7.7 \times 10^{-6} \ll 1 \quad (95)$$

where R is the radius of the solidified track, $\Delta\rho$ is the difference between the solid and liquid densities, and γ is the fluid surface tension.

Since $Bd \ll 1$, the gravitational forces are negligible, and the track shape is primarily determined by surface tension, resulting in a circular cross-section.

The track width, which is determined by the melt pool width, remains constant before and after solidification. The solid contact angle is 96°. The densities of solid and liquid Inconel 625 are 8567 kg/m^3 and 7680 kg/m^3, respectively. Consequently, the ratio of the liquid volume fraction to the solid volume fraction, which is based on Eq. (32), is as follows:

$$\frac{\varphi_l}{\varphi_s} = \frac{\rho_s}{\rho_l} = \frac{8567}{7680} = 1.115$$

Given a solid contact angle of 96°, $\varphi_s = 0.45$. Therefore:

$$\varphi_l = 1.115 \times 0.45 = 0.5$$

From supplementary Table S1, the liquid wetting angle is 100.5°. The solid height of the track in Fig. 9 is 175 μm, and the height of the liquid, which is based on Eq. (34), is as follows:

$$H_l = 175\left(\frac{\cot\left(\frac{96^\circ}{2}\right)}{\cot\left(\frac{100.5^\circ}{2}\right)}\right) = 190\,\mu\text{m}$$

To calculate the β angle (melt pool boundary angle inside the substrate):

$$\beta = \sqrt{2}\tan^{-1}\left(\frac{166}{156}\right) = 66^\circ$$

These calculations provide valuable insights into the wetting behavior of solid-liquid transformation during the solidification of tracks.

Conclusion

This work presents a comprehensive mathematical framework that significantly advances our understanding of track formation in AM. By establishing robust quantitative relationships between process parameters and track geometry, the framework enables precise prediction and optimization of key track attributes, thereby enhancing the quality and repeatability of AMed parts. The key contributions of this study include the following:

- **Accurate wetting behavior prediction:** By deriving explicit relationships between track width, height, and contact angle, the framework accurately determines solid and liquid wetting angles for acute and obtuse scenarios, effectively mitigating errors common in traditional methods.
- **Dimensionless wetting shape factors:** Introducing dimensionless shape factors for width, height, and radius facilitates the accurate calculation of track area and volume, providing essential tools for process design.
- **Correlation with powder layer thickness:** The development of quadratic equations that relate powder layer thickness to track dimensions—while incorporating powder properties—offers critical insights into forming the initial single track.
- **Combined geometric modeling:** A novel fitting model that employs a circular approximation for the upper surface of the track and a parabolic model for its depth, coupled with established relationships between NE, track depth, and absorption, provides a robust predictive tool for tailoring track geometry based on process parameters.
- **Transition analysis:** The framework elucidates the transition from initial single-track behavior—where the track height exceeds the powder layer thickness—to a steady-state regime where the track height aligns with the effective powder layer thickness. In addition, it offers an in-depth examination of the evolution of wetting behavior from the liquid state to the solid state.
- **Optimal hatch spacing determination:** Three distinct equations for determining the optimal hatch spacing—derived from single-track and steady-state attributes—ensure sufficient overlap between adjacent tracks, thus preventing the lack of fusion and minimizing defects.

Experimental validation across diverse materials and processing conditions confirms the predictive accuracy of the models. Although primarily developed for LPBF, these equations' fundamental principles broadly apply to other AM processes, such as electron beam powder bed fusion (EB-PBF) and direct energy deposition (DED).

Integrating this framework with advanced machine learning techniques could enable real-time monitoring and predictive control of track formation. Such integration promises to serve as a cornerstone for comprehensive process modeling and optimization in AM, offering enhanced control over track formation and ultimately facilitating more precise and reliable manufacturing outcomes.

Methods

A Concept Laser M2 system with a Yb-fiber laser produced single-track samples to validate our mathematical model. The laser, which features a Gaussian beam profile, delivers beam diameters of 100 μm and 120 μm at the surface, depending on the specific process settings. The build plate was preheated to 80 °C for processing IN625 and IN738LC alloys and to 200 °C for the AA1000 and Al10SiMg materials.

The metal powders, possessing nominal standard chemical compositions, exhibited a particle size distribution with D_{10}, D_{50}, and D_{90} values of 23 μm, 33 μm, and 47 μm, respectively. Single tracks were fabricated on the top surface after 100 layers were printed via a stripe scan strategy. These tracks were printed with varying powder thicknesses to validate the governing equations under different conditions. Each track was printed twice to ensure reproducibility.

After printing, the sample was sectioned along its transverse plane to facilitate a detailed melt pool examination. The samples were then polished and chemically etched via standard metallographic procedures, revealing the melt pool morphology and associated features. The melt pool attributes were subsequently characterized by scanning electron microscopy with a Hitachi SU5000 and optical imaging with a Leica DMI 5000 M microscope. This systematic approach enables a comprehensive analysis of single-track geometries and microstructures, thereby validating the mathematical models developed in this study.

Data availability

All datasets generated and analyzed throughout this work are available from the corresponding author upon reasonable request.

Received: 18 June 2025; Accepted: 23 June 2025;
Published online: 08 July 2025

References

1. Mukherjee, T. & DebRoy, T. Mitigation of lack of fusion defects in powder bed fusion additive manufacturing. *J. Manuf. Process.* **36**, 442–449 (2018).
2. de Formanoir, C. et al. Healing of keyhole porosity by means of defocused laser beam remelting: operando observation by x-ray imaging and acoustic emission-based detection. *Addit. Manuf.* **79**, 103880 (2024).
3. Queva, A., Guillemot, G., Moriconi, C., Bergeron, R. & Bellet, M. Mesoscale multilayer multitrack modeling of melt pool physics in laser powder bed fusion of lattice metal features. *Addit. Manuf.* 104365 https://linkinghub.elsevier.com/retrieve/pii/S2214860424004111 (2024).
4. Bhatt, A. et al. In situ characterisation of surface roughness and its amplification during multilayer single-track laser powder bed fusion additive manufacturing. *Addit. Manuf.* **77**, 103809 (2023).
5. Lu, L. X. et al. Integrated modelling and simulation of Niti alloy by powder bed fusion: single track study. *Mater. Design* **227**, 111755(2023).
6. William, F. T., Shawn, H., Seth, S., Albert, T. & Prabha, N. S. Finding the limits of single-track deposition experiments: an experimental study of melt pool characterization in laser powder bed fusion. *Mater. Design* **231**, 112069 (2023).
7. Tang, M., Pistorius, P. C. & Beuth, J. L. Prediction of lack-of-fusion porosity for powder bed fusion. *Addit. Manuf.* **14**, 39–48 (2017).
8. Kumar, P., Jain, N. K. & Sawant, M. S. Development of theoretical models for dimensions of single-layer multi-track and multi-layer multi-track depositions by μ-pta additive manufacturing process. *J. Mater. Res. Technol.* **17**, 95–110 (2022).
9. Yan, W. et al. Multi-physics modeling of single/multiple-track defect mechanisms in electron beam selective melting. *Acta Mater.* **134**, 324–333 (2017).
10. Agrawal, A. K., Rankouhi, B. & Thoma, D. J. Predictive process mapping for laser powder bed fusion: a review of existing analytical solutions. *Curr. Opin. Solid State Mater. Sci.* **26**, 101024 (2022).
11. Rosenthal, B. D. The theory of moving sources of heat and its application to metal treatments http://asmedigitalcollection.asme.org/fluidsengineering/article-pdf/68/8/849/6963474/849_1.pdf (1946).
12. Eagar, T. W. & Tsai, N. S. Temperature fields produced by traveling distributed heat sources. *Weld. Res. Suppl.* **62**, 346–355 (1983).
13. Hann, D. B., Iammi, J. & Folkes, J. A simple methodology for predicting laser-weld properties from material and laser parameters. *J. Phys. D Appl. Phys.* **44**, 445401 (2011).
14. Ghasemi-Tabasi, H. et al. An effective rule for translating optimal selective laser melting processing parameters from one material to another. *Addit. Manuf.* **36**, 101496 (2020).
15. King, W. E. et al. Observation of keyhole-mode laser melting in laser powder-bed fusion additive manufacturing. *J. Mater. Process. Technol.* **214**, 2915–2925 (2014).
16. Xu, Y. et al. Single-track investigation of additively manufactured mold steel with larger layer thickness processing: track morphology, melt pool characteristics and defects. *Opt. Laser Technol.* **171**, 110378 (2024).
17. Huhtamäki, T., Tian, X., Korhonen, J. T. & Ras, R. H. Surface-wetting characterization using contact-angle measurements. *Nat. Protoc.* **13**, 1521–1538 (2018).
18. Zhang, B. et al. An efficient framework for printability assessment in laser powder bed fusion metal additive manufacturing. *Addit. Manuf.* **46**, 102018 (2021).
19. Bäuerle, D. *Laser processing and chemistry* (Springer Science & Business Media, 2013).
20. Steen, W. M. & Mazumder, J. *Laser Material Processing* (Springer Science & Business Media, 2010).
21. Bejan, A. *Convection Heat Transfer* (John Wiley & Sons, 2013).
22. Gaskell, D. R. & Laughlin, D. E. *Introduction to the Thermodynamics of Materials* (CRC Press, 2017).
23. Andersson, J. O., Helander, T., Höglund, L., Shi, P. & Sundman, B. Thermo-Calc & DICTRA, computational tools for materials science. *Calphad* **26**, 273–312 (2002).
24. Sow, M. et al. Influence of beam diameter on laser powder bed fusion (L-PBF) process. *Addit. Manuf.* **36**, 101532 (2020).

Acknowledgements

This work was supported by funding from the European Union's Horizon 2020 Research and Innovation Programme under the Marie Skłodowska-Curie Grant Agreement No. 101034425 for the A2M2TECH project. Additional funding for the A2M2TECH project was provided by the Scientific and Technological Research Council of Türkiye (TÜBİTAK) under Grant No. 120C158 through the TÜBİTAK 2236/B Program. Furthermore, this work also received funding from TÜBİTAK under Grant No. 20AG008 through the TÜBİTAK 1004 Program.

Author contributions

Mahdi Alishavandi: writing—original draft, writing—review and editing, investigation, data curation, conceptualization, visualization, methodology, formal analysis, validation. Metin U. Salamci: supervision, project administration, funding acquisition. Rahmi Ünal: supervision.

Competing interests

The authors declare no competing interests.

Additional information

Supplementary information The online version contains supplementary material available at https://doi.org/10.1038/s43246-025-00862-8.

Correspondence and requests for materials should be addressed to Mahdi Alishavandi.

Peer review information *Communications Materials* thanks the anonymous reviewers for their contribution to the peer review of this work. Primary handling editor: John Plummer. A peer review file is available.

Reprints and permissions information is available at http://www.nature.com/reprints

Publisher's note Springer Nature remains neutral with regard to jurisdictional claims in published maps and institutional affiliations.

Open Access This article is licensed under a Creative Commons Attribution 4.0 International License, which permits use, sharing, adaptation, distribution and reproduction in any medium or format, as long as you give appropriate credit to the original author(s) and the source, provide a link to the Creative Commons licence, and indicate if changes were made. The images or other third party material in this article are included in the article's Creative Commons licence, unless indicated otherwise in a credit line to the material. If material is not included in the article's Creative Commons licence and your intended use is not permitted by statutory regulation or exceeds the permitted use, you will need to obtain permission directly from the copyright holder. To view a copy of this licence, visit http://creativecommons.org/licenses/by/4.0/.

© The Author(s) 2025